3D vs. 2D Channel Models: Spatial Correlation and Channel Capacity Comparison and Analysis

Yawei Yu*, Peter J. Smith†, Pawel A. Dmochowski†, Jianhua Zhang* and Mansoor Shafi‡
*Beijing University of Posts and Telecommunications, Beijing, China.
†Victoria University of Wellington, Wellington, New Zealand.
‡Spark New Zealand, Wellington, New Zealand.
Email: {yyw,jhzhang}@bupt.edu.cn, {peter.smith,pawel.dmochowski}@vuw.ac.nz, mansoor.shafi@spark.co.nz

***Abstract*—Results of recent measurement campaigns demonstrate a significant increase in the degrees of freedom introduced by the elevation domain, and consequently, a large capacity gap as predicted by 3D and 2D MIMO channel models. To gain further insight into the effects of the elevation domain on MIMO system performance, we derive new spatial correlation (SC) expressions for 3D and 2D channel models, given rectangular arrays of cross-polarized antennas. The main result relates 3D SC to the 2D counterpart, allowing us to quantify the effects of the elevation domain on SC. Furthermore, our result allows us to derive the following three simple relationships between 2D and 3D correlations. We show that for a small elevation angle spread, the difference between 2D and 3D SCs grows quadratically in both vertical separation and angle spread. For the case of small vertical spacings, we derive a bound on the above correlation gap. Furthermore, we show that the elevation effects on correlation can be accurately decoupled, allowing us to express the 3D SC matrix as a Hadamard product of a 2D SC matrix and an elevation component. Collectively, our results demonstrate the need for accurate channel modeling when evaluating the performance of 3D MIMO systems.**

I. Introduction

With the proliferation of mobile devices and applications, it is estimated that global International Mobile Telecommunications (IMT) traffic will grow 10-100 times between 2020 and 2030 [1]. To meet these requirements, new technologies such as large antenna arrays (massive MIMO) are being investigated. Since such antenna arrays utilize both the azimuth and elevation domain, three dimensional (3D) MIMO channel models are being investigated and standardized for 5th generation (5G) mobile communication system [2]. Recently, the 3rd Generation Partnership Project (3GPP) has released the 3D channel model [3] as an extension of the conventional 2D model [4]. Simulation results based on these models [5] as well as field measurements [6] have shown that utilizing the elevation domain results in significantly larger channel capacity.

It is well known that the presence of spatial correlation (SC) between antenna elements reduces the spectral efficiency of a MIMO system. As such, understanding antenna SC allows a more accurate prediction of the system performance. Much of the work on SC ignores the elevation domain due to simplicity and the lack of standardized 3D models [7], [8]. SC for 3D propagation was considered by modeling the distribution of scatterers with a von Mises-Fisher distribution [9]. Here, the authors also derive an expression for the SC function based on a spherical harmonic expansion. Closed form expressions for 3D SC for different angle distributions are investigated in [10]. Very recently, a general method for deriving a closed form expression for 3D SC was proposed in [11]. This method, valid for arbitrary angular distributions, also uses a spherical harmonic expansion of plane waves to produce an expression utilizing the Fourier Series expansion of the power azimuth and elevation spectra.

In this paper, we present new results on antenna SC for a 3D MIMO channel model. The two distinguishing features of our results in contrast to [9]–[11] are as follows. First, our model considers a rectangular array of cross-polarized antennas - a feature of most recent standards documents [3], [4]. More importantly, the complex expressions in [9]–[11] do not offer clear insight into the effects of the elevation domain on SC. Since quantifying this effect is the precise aim of the work, we derive new expressions which explicitly relate the correlation of a 3D MIMO channel model to that of a classic, 2D model. Specifically, the contributions of this work can be summarized as follows:

- Motivated by the channel capacity gain from 2D MIMO to 3D MIMO observed in measurements (demonstrated in [6], see Fig. 1), we derive new expressions for the SC between antenna elements based on 2D and 3D models. The expressions allow us to derive the relationship between the 2D and 3D SCs (Section III-C).
- Using the above results, we investigate the effects of 3D modeling on SC for different scenarios. Results (both via simulation and analysis) show that 3D SC decreases rapidly with vertical spacing, and will be much lower than 2D SC except for small vertical

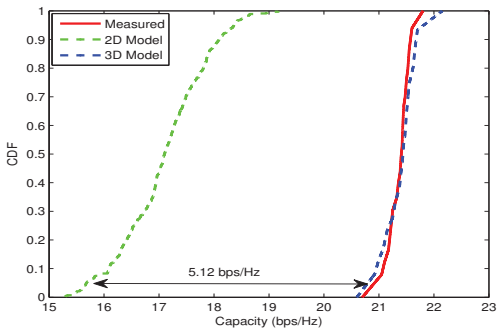

Fig. 1. Channel Capacity CDF (SNR=5 dB): Measurements reported in [6]

978-1-4673-8999-0/17/$31.00 ©2017 IEEE

spacing where 3D SC can exceed 2D SC (Section IV-A).

- We derive simple expressions for the difference between 3D and 2D SCs for narrow elevation angle spread as well as for small vertical separation (Section IV-B). In the case of the former, we learn that the SC difference increases quadratically with the elevation interval spacing and elevation angle spread. These simple, closed form results allow us to quantify the effect of the elevation domain on antenna SC.
- We derive an expression which decouples the SC due to elevation from that of a 2D model, thus approximating the 3D SC matrix as a Hadamard product of a 2D SC matrix and an elevation component, in turn allowing for a simpler calculation of 3D SC. (Section IV-C).

Collectively, the above findings highlight the importance of accurate 3D channel modeling on performance analysis of MIMO systems. We include capacity results in support of this (Section IV-D).

Notation: $\odot, \otimes, (\cdot)^T, (\cdot)^H$ denote the Hadamard product, Kronecker product, the transpose and conjugate transpose, respectively. $J_0(\cdot)$, $\mathcal{U}(a,b)$ and $\mathcal{CN}(0,\gamma_c^2 c)$ denote the zeroth order modified Bessel function of the first kind, uniform distribution within (a,b) and a complex normal distribution with zero mean and γ_c^2 variance, respectively.

II. Channel Model

We consider a MIMO system with M antennas in the transmitter (Tx) and Q antennas in the receiver (Rx), where the Tx and Rx each employ a rectangular array with cross polarized antennas, in the y-z plane, shown in Fig. 2. The interval spacing between adjacent patches of cross polarization pairs is denoted by dy and dz. The elevation/azimuth angles of incoming/outgoing rays are denoted by θ and ϕ, respectively.

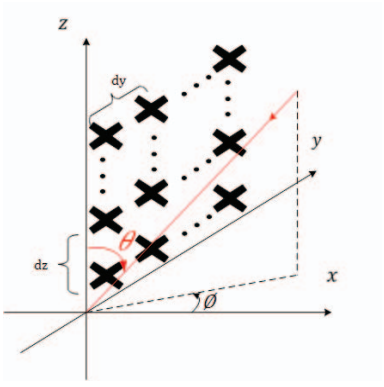

Fig. 2. Rectangular antenna array with cross polarized antenna pairs

The channel impulse response (CIR) between the q^{th} Rx element and the m^{th} Tx element is given by [3], [4]

$$h_{q,m} = \frac{1}{\sqrt{L}} \sum_{c=1}^{C} \sum_{l=1}^{L} g_{c,l} \begin{bmatrix} F_{\text{Rx},q,V}^{c,l} \\ F_{\text{Rx},q,H}^{c,l} \end{bmatrix}^T \begin{bmatrix} \alpha_{VV}^{c,l} & \alpha_{VH}^{c,l} \\ \alpha_{HV}^{c,l} & \alpha_{HH}^{c,l} \end{bmatrix} \begin{bmatrix} F_{\text{Tx},m,V}^{c,l} \\ F_{\text{Tx},m,H}^{c,l} \end{bmatrix} \times \exp\left(j2\pi \boldsymbol{r}_{\text{Rx},c,l}^T \boldsymbol{d}_q\right) \exp\left(j2\pi \boldsymbol{r}_{\text{Tx},c,l}^T \boldsymbol{d}_m\right), \tag{1}$$

where

- $c \in \{1,2,...,C\}$ and $l \in \{1,2,...,L\}$ denote the cluster and subpath indices, respectively.
- $F_{\text{Rx},q,V}^{c,l}, F_{\text{Rx},q,H}^{c,l}$ are the q^{th} Rx element field patterns for vertical and horizontal polarizations of subpath l in cluster c, respectively.
- $F_{\text{Tx},m,V}^{c,l}, F_{\text{Tx},m,H}^{c,l}$ are the m^{th} Tx element field patterns for vertical and horizontal polarizations of subpath l in cluster c, respectively.
- $\alpha_{VV}^{c,l}, \alpha_{VH}^{c,l}, \alpha_{HV}^{c,l}, \alpha_{HH}^{c,l}$ are the complex gains of vertical-to-vertical, horizontal-to-vertical, vertical-to-horizontal and horizontal-to-horizontal polarizations of subpath l in cluster c, respectively.
- $\boldsymbol{r}_{\text{Rx},c,l}, \boldsymbol{r}_{\text{Tx},c,l}$ denote the spherical unit vectors of the received and transmitted subpath l in cluster c, respectively.
- $\boldsymbol{d}_q, \boldsymbol{d}_m$ are the location vectors for the q^{th} Rx element and m^{th} Tx element, measured in wavelengths, λ_0, of the carrier frequency.
- $g_{c,l}$ is the complex amplitude of subpath l in cluster c with a distribution $\mathcal{CN}(0,\gamma_c^2)$, γ_c^2 is the fraction of total power contained in cluster c, i.e., $E[\gamma_c^2] = \frac{1}{C}$.

A. 3D Channel Model

Taking the elevation domain into consideration, the parameters of the 3D model in (1) are given by [3]

$$\begin{bmatrix} F_{\text{Rx},q,V}^{c,l} \\ F_{\text{Rx},q,H}^{c,l} \end{bmatrix}^T = \begin{bmatrix} \sqrt{A(\vartheta_{c,l},\varphi_{c,l})}\cos(\xi_q) \\ \sqrt{A(\vartheta_{c,l},\varphi_{c,l})}\sin(\xi_q) \end{bmatrix}^T, \tag{2}$$

$$\begin{bmatrix} \alpha_{VV}^{c,l} & \alpha_{VH}^{c,l} \\ \alpha_{HV}^{c,l} & \alpha_{HH}^{c,l} \end{bmatrix} = \begin{bmatrix} e^{j\Phi_{VV}^{c,l}} & \sqrt{\kappa^{-1}} e^{j\Phi_{VH}^{c,l}} \\ \sqrt{\kappa^{-1}} e^{j\Phi_{HV}^{c,l}} & e^{j\Phi_{HH}^{c,l}}, \end{bmatrix} \tag{3}$$

$$\boldsymbol{r}_{\text{Rx},c,l} = [\sin(\vartheta_{c,l})\cos(\varphi_{c,l}), \sin(\vartheta_{c,l})\sin(\varphi_{c,l}), \cos(\vartheta_{c,l})]^T, \tag{4}$$

$$\boldsymbol{d}_q = (dx_q, dy_q, dz_q)^T, \tag{5}$$

where

- $A(\vartheta_{c,l},\varphi_{c,l})$ is the antenna field pattern at the Rx

$$A(\vartheta_{c,l},\varphi_{c,l}) = -\min\left\{-[A_V(\vartheta_{c,l}) + A_H(\varphi_{c,l})], A_m\right\}, \tag{6}$$

with

$$A_V(\vartheta_{c,l})\text{ dB} = -\min\left[12(\frac{\vartheta_{c,l} - 90^o}{\vartheta_{3dB}})^2, SLA_v\right], \quad \vartheta_{3\text{dB}} = 65^o, \quad SLA_v = 30\text{ dB}. \tag{7}$$

and

$$A_H(\varphi_{c,l})\text{ dB} = -\min\left[12(\frac{\varphi_{c,l}}{\varphi_{3\text{ dB}}})^2, A_m\right], \quad \varphi_{3\text{dB}} = 65^o, \quad A_m = 30\text{ dB}. \tag{8}$$

- ξ_q, ξ_m are the polarization slant angles of the q^{th} Rx element and m^{th} Tx element, respectively.

- $\Phi_{VV}^{c,l}, \Phi_{VH}^{c,l}, \Phi_{HV}^{c,l}, \Phi_{HH}^{c,l}$ are the random initial phases for four different polarization combinations VV, VH, HV, HH for subpath l in cluster c. The initial phases are assumed to be uniformly distributed on $(-\pi, \pi)$.
- κ is the cross polarization power ratio.

As the rectangular array is placed at y-z plane, the location vector for the q^{th} Rx antenna, $\boldsymbol{d}_q$, will be $(0, dy_q, dz_q)^T$. The analogous definitions for the Tx parameters are obtained by substituting $\{\theta_{c,l}, \phi_{c,l}, \xi_m\}$ for $\{\vartheta_{c,l}, \varphi_{c,l}, \xi_q\}$ in (2)-(8).

B. 2D Channel Model

The conventional 2D channel model assumes that the signal propagates in a plane effectively disregarding the elevation angle. The parameters for the resulting 2D model are given by [4]

$$\begin{bmatrix} F_{\mathrm{Rx},q,V}^{c,l} \\ F_{\mathrm{Rx},q,H}^{c,l} \end{bmatrix}^T = \begin{bmatrix} \sqrt{A_H(\varphi_{c,l})}\cos(\xi_q) \\ \sqrt{A_H(\varphi_{c,l})}\sin(\xi_q) \end{bmatrix}^T, \tag{9}$$

$$\boldsymbol{r}_{\mathrm{Rx},c,l} = [\cos(\varphi_{c,l}), \sin(\varphi_{c,l})]^T, \tag{10}$$

$$\boldsymbol{d}_q = (dx_q, dy_q)^T. \tag{11}$$

In (9), $A_H(\varphi_{c,l})$ denotes the antenna field pattern in the azimuth domain, given by (8). The analogous expressions for the Tx parameters are obtained by replacing $\{\varphi_{c,l}, \xi_q\}$ with $\{\phi_{c,l}, \xi_m\}$ in (9)-(10).

III. Channel Correlation: Analytical Expressions

We now derive the expressions for the SC between antenna element pairs. The SC for the 3D and 2D models are given in Section III-A and Section III-B, respectively, while the relationship between the two is derived in Section III-C.

A. 3D Correlation Calculation

Let $\{q, q_\perp\}$ denote pairs of cross-polarized, co-located antenna elements. Substituting the parameters for the 3D channel model in (2-8) into (1), the CIR between the q^{th} cross-polarized Rx element pair and the m^{th} Tx element can be rewritten as

$$\begin{cases} h_{q,m} = \dfrac{1}{\sqrt{L}}\displaystyle\sum_{c=1}^{C}\sum_{l=1}^{L} g_{c,l}\sqrt{A(\theta_{c,l},\phi_{c,l})A(\vartheta_{c,l},\varphi_{c,l})}P_{q,m} \\ \qquad\qquad \times e^{(j2\pi \boldsymbol{r}_{\mathrm{Rx},c,l}^T \boldsymbol{d}_q)} e^{(j2\pi \boldsymbol{r}_{\mathrm{Tx},c,l}^T \boldsymbol{d}_m)} \\ h_{q_\perp,m} = \dfrac{1}{\sqrt{L}}\displaystyle\sum_{c=1}^{C}\sum_{l=1}^{L} g_{c,l}\sqrt{A(\theta_{c,l},\phi_{c,l})A(\vartheta_{c,l},\varphi_{c,l})}P_{q_\perp,m} \\ \qquad\qquad \times e^{(j2\pi \boldsymbol{r}_{\mathrm{Rx},c,l}^T \boldsymbol{d}_{\perp,q})} e^{(j2\pi \boldsymbol{r}_{\mathrm{Tx},c,l}^T \boldsymbol{d}_m)}, \end{cases} \tag{12}$$

where

$$\begin{cases} P_{q,m} = \cos(\xi_q)[\alpha_{VV}^{c,l}\cos(\xi_m) + \alpha_{VH}^{c,l}\sin(\xi_m)] + \\ \qquad \sin(\xi_q)[\alpha_{HV}^{c,l}\cos(\xi_m) + \alpha_{HH}^{c,l}\sin(\xi_m)] \\ P_{q_\perp,m} = -\sin(\xi_q)[\alpha_{VV}^{c,l}\cos(\xi_m) + \alpha_{VH}^{c,l}\sin(\xi_m)] + \\ \qquad \cos(\xi_q)[\alpha_{HV}^{c,l}\cos(\xi_m) + \alpha_{HH}^{c,l}\sin(\xi_m)]. \end{cases} \tag{13}$$

The vector of CIRs between the m^{th} Tx element and all Rx elements is thus

$$\boldsymbol{h}_m = \frac{1}{\sqrt{L}}\sum_{c=1}^{C}\sum_{l=1}^{L} g_{c,l}\sqrt{A(\theta_{c,l},\phi_{c,l})A(\vartheta_{c,l},\varphi_{c,l})} \times \boldsymbol{a}_{Rx} \otimes [P_{q,m}, P_{q_\perp,m}]^T e^{j2\pi \boldsymbol{r}_{\mathrm{Tx},c,l}^T \boldsymbol{d}_m}, \tag{14}$$

where the $\frac{Q}{2} \times 1$ vector $\boldsymbol{a}_{\mathrm{Rx}}$ is given by

$$\boldsymbol{a}_{\mathrm{Rx}} = \left[e^{j2\pi \boldsymbol{r}_{\mathrm{Rx},c,l}^T \boldsymbol{d}_1}, e^{j2\pi \boldsymbol{r}_{\mathrm{Rx},c,l}^T \boldsymbol{d}_2}, ..., e^{j2\pi \boldsymbol{r}_{\mathrm{Rx},c,l}^T \boldsymbol{d}_{\frac{Q}{2}}} \right]^T. \tag{15}$$

Using (14) and noting that elements of $\boldsymbol{h}_m$ have zero mean, we compute the SC between transmitter elements m and m' using

$$R_{mm'}^{\mathrm{3D}} = \frac{\mathbb{E}\{\boldsymbol{h}_m^* \boldsymbol{h}_{m'}\}}{\sqrt{\mathbb{E}\{||\boldsymbol{h}_m||^2\}\mathbb{E}\{||\boldsymbol{h}_{m'}||^2\}}}. \tag{16}$$

In Appendix A, we show that the SC, $R_{mm'}^{\mathrm{3D}}$ in (16), can be simplified to

$$R_{mm'}^{\mathrm{3D}} = \begin{cases} \dfrac{\mathbb{E}\{A(\theta,\phi)e^{-j2\pi \boldsymbol{r}_{\mathrm{Tx}}^T(\boldsymbol{d}_m - \boldsymbol{d}_{m'})}\}}{\mathbb{E}\{A(\theta,\phi)\}} & \text{for } \xi_m = \xi_{m'}, \\ 0 & \text{for } |\xi_m - \xi_{m'}| = \pi/2. \end{cases} \tag{17}$$

B. 2D Correlation Calculation

The SC expression for the 2D model can easily be obtained by simplifying (17), resulting in

$$R_{mm'}^{\mathrm{2D}} = \begin{cases} \dfrac{\mathbb{E}\{A_H(\phi)e^{-j2\pi \boldsymbol{r}_{\mathrm{Tx}}^T(\boldsymbol{d}_m - \boldsymbol{d}_{m'})}\}}{E\{A_H(\phi)\}} & \text{for } \xi_m = \xi_{m'}, \\ 0 & \text{for } |\xi_m - \xi_{m'}| = \pi/2. \end{cases} \tag{18}$$

C. Relationship between 2D and 3D Correlation

We now derive the relationship between (17) and (18) which subsequently will be used to quantify the effects of including the elevation domain on antenna SC. Assuming θ and ϕ are independent variables and approximating

$$A(\theta,\phi) = A_V(\theta)A_H(\phi), \tag{19}$$

(17) can be further simplified to

$$R_{mm'}^{\mathrm{3D}} = \begin{cases} \dfrac{\mathbb{E}\{A_V(\theta)A_H(\phi)e^{-j2\pi \boldsymbol{r}_{\mathrm{Tx}}^T(\boldsymbol{d}_m - \boldsymbol{d}_{m'})}\}}{\mathbb{E}\{A_V(\theta)\}\mathbb{E}\{A_H(\phi)\}} & \text{for } \xi_m = \xi_{m'}, \\ 0 & \text{for } |\xi_m - \xi_{m'}| = \pi/2. \end{cases} \tag{20}$$

1) The case of $|\xi_m - \xi_{m'}| = \pi/2$, i.e., when we consider antennas with opposite polarization, gives the obvious relationship of $R_{mm'}^{\mathrm{3D}} = R_{mm'}^{\mathrm{2D}} = 0$;
2) When $\xi_m = \xi_{m'}$, substituting (4) and (5) into (20) gives

$$R_{mm'}^{\mathrm{3D}}(dx,dy,dz) = \mathbb{E}_\theta\left\{A_V(\theta)e^{-j2\pi dz\cos\theta}\mathbb{E}_\phi\{A_H(\phi) e^{-j2\pi(dx\sin\theta\cos\phi + dy\sin\theta\sin\phi)}\}\right\} / \left\{\mathbb{E}\{A_V(\theta)\}\mathbb{E}\{A_H(\phi)\}\right\}, \tag{21}$$

where we explicitly parameterize $R_{mm'}^{\mathrm{3D}}$ by the spacing (dx, dy, dz) between the Tx antenna m and m' to aid subsequent analysis. Similarly, substituting (10) and (11) into (18)

gives

$$R^{\text{2D}}_{mm'}(dx,dy)=\frac{\mathbb{E}_{\phi}\{A_H(\phi)e^{-j2\pi(dx\cos\phi+dy\sin\phi)}\}}{\mathbb{E}\{A_H(\phi)\}}. \quad (22)$$

Comparing (21) with (22), we note that

$$R^{\text{3D}}_{mm'}(dx,dy,dz) = \frac{\mathbb{E}_{\theta}\{R^{\text{2D}}_{mm'}(dx\sin\theta,dy\sin\theta)A_V(\theta)e^{-j2\pi dz\cos\theta}\}}{\mathbb{E}\{A_V(\theta)\}}. \quad (23)$$

When $dz=0$ and $\theta=\pi/2$, (23) will be simplified as $R^{\text{3D}}_{mm'}(dx,dy,0)$=$R^{\text{2D}}_{mm'}(dx,dy)$, showing that 2D SC is a special case of 3D SC. In the following section, (23) will be used to derive further results giving new insights into $R^{\text{2D}}_{mm'}$ and $R^{\text{3D}}_{mm'}$ for specific scenarios.

IV. Results and Analysis

The relationship between the spatial SC predicted by 2D and 3D models in (23) enables us to derive a number of insights into the effects of channel modeling on antenna SC. This is the focus of Section IV, where we present a series of simulation results in support of (23), and derive additional analytical results for antenna SC for a number of special cases considered.

A. $R^{3D}_{mm'}$ and $R^{2D}_{mm'}$ Comparison

Figures 3a) and 3b) show the SC between antenna elements computed using (17) and (18) as a function of the spacing in the y- and z- directions, respectively. We consider different scenarios as given in the legend. In all cases, the separation in the x-direction is fixed to $dx=0$, i.e., we consider a rectangular array in the yz plane, as shown in Fig. 2.

Fig. 3a) demonstrates a rapid decrease in the SC as the separation dy increases, reaching 0 for $dy\approx 1\lambda$ for both models. For the 3D model and $dy=0$, increasing the vertical separation from $dz=0$ to $dz=0.5\lambda$ reduces the 3D SC by a factor of 2, i.e., significantly below that predicted by the 2D model. This effect is also evident in Fig. 3b), where the SC is plotted as a function of dz.

We also observe from Fig. 3a) that 3D SC $R^{\text{3D}}_{mm'}$ can be larger than 2D SC $R^{\text{2D}}_{mm'}$ for $dz=0$, in particular for a wide elevation angular spread ($\theta\sim U(0,180^o)$). This is also evident in Fig. 3b) for small values of dz. This gap diminishes for a narrower elevation angle spread ($\theta\sim U(80^o,100^o)$), and becomes zero for $\theta=90^o$. This phenomenon can be verified by examining (23) with $dz=0$ and for simplicity, $A_V(\theta)=1$ (that is, ignoring the effects of antenna radiation pattern, the effects of which are examined later). Here,

$$\begin{aligned}R^{\text{3D}}_{mm'}(dx,dy,0) &= R^{\text{2D}}_{mm'}(dx\sin\theta,dy\sin\theta)\\ &\geq R^{\text{2D}}_{mm'}(dx,dy),\end{aligned} \quad (24)$$

where the second equality holds for $\theta=90^o$, otherwise $R^{\text{3D}}_{mm'}>R^{\text{2D}}_{mm'}$. (24) shows that the 3D SC at a spacing of (dx,dy) is equivalent to 2D SC with a reduced spacing of $(dx\sin\theta,dy\sin\theta)$, thus 3D SC is larger than 2D SC. When θ approches 90^o, the equivalent space $(dx\sin\theta,dy\sin\theta)$ gets closer to (dx,dy), thus the gap between 3D SC and 2D SC diminishes to 0.

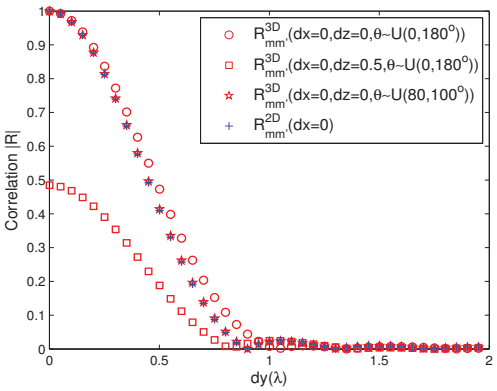

(a) $R^{\text{3D}}_{mm'}$ and $R^{\text{2D}}_{mm'}$ vs. dy

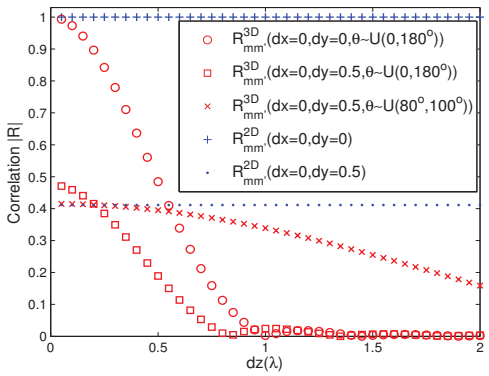

(b) $R^{\text{3D}}_{mm'}$ and $R^{\text{2D}}_{mm'}$ vs. dz

Fig. 3. Spatial SC based on 2D and 3D models vs. different interval spacing

Next, we examine the effects of the antenna radiation pattern in the elevation domain. Fig. 4 shows the SC as a function of dy with a constant $A_V(\theta)$ and that given by (8). We note a great discrepancy between the SC values, where the 3D model with the elevation antenna pattern is significantly lower. Thus, as with increasing dz, the elevation antenna pattern reduces the SC predicted by the 3D model, resulting in $R^{\text{3D}}_{mm'}<R^{\text{2D}}_{mm'}$.

B. $R^{2D}_{mm'}$ and $R^{3D}_{mm'}$ Gap

Equation (23) allows us to quantify the discrepancy between $R^{\text{3D}}_{mm'}$ and $R^{\text{2D}}_{mm'}$ for the scenarios of small elevation angle spread and small elevation interval dz. Those results are presented in the following two lemmas.

Lemma 1: For narrow elevation angle spread, that is $\theta\sim\mathcal{U}(\frac{\pi}{2}-\varepsilon,\frac{\pi}{2}+\varepsilon)$ for $0<\varepsilon\ll 1$,

$$\begin{aligned}R^{\text{2D}}_{mm'}(dx,dy)-R^{\text{3D}}_{mm'}(dx,dy,dz)\\ \approx\frac{2\pi^2dz^2\varepsilon^2}{3}R^{\text{2D}}_{mm'}(dx,dy).\end{aligned} \quad (25)$$

Proof: See Appendix B.

Thus, the relative difference in the SC obtained from the two channel models is proportional to the square of both the vertical separation dz and elevation angle spread ε.

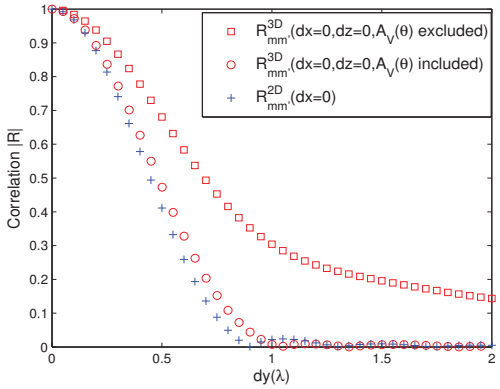

Fig. 4. $R^{3D}_{mm'}$ and $R^{2D}_{mm'}$ vs dy with and without $A_V(\theta)$

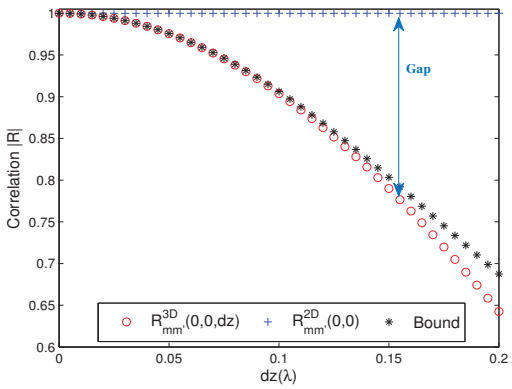

Fig. 6. Channel Correlation Variation with dz

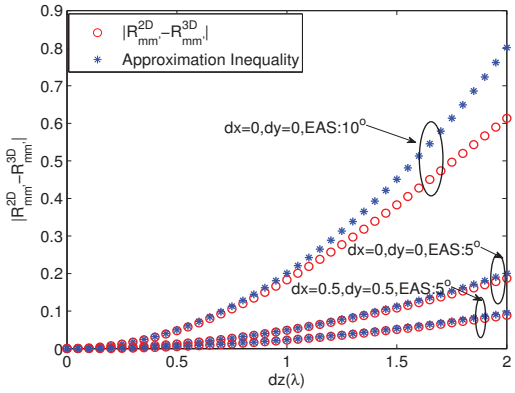

Fig. 5. Correlation gap and the approximation in (25)

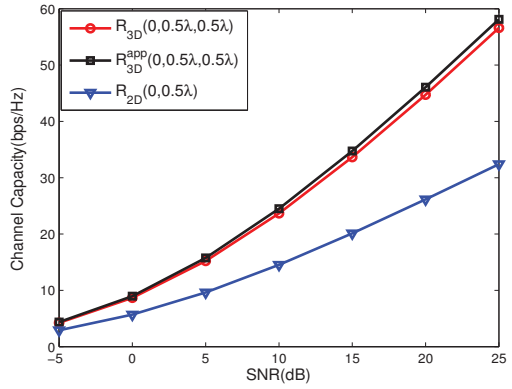

Fig. 7. Channel capacity of 8× 8 MIMO system for $\mathbf{R}_{2D}, \mathbf{R}_{3D}$ and $\mathbf{R}^{app}_{3D}$

This relationship is verified in Fig. 5, which shows the true difference $R^{3D}_{mm'} - R^{2D}_{mm'}$ and that approximated in (25) for $\varepsilon = 5^o$, $\varepsilon = 10^o$ and $dy = 0$, $dy = 0.5$. We note very good agreement in the true simulated and approximate analytical results for $\varepsilon = 5^o$.

Lemma 2: For $dx = 0$, $dy = 0$ (i.e., for vertical separation only), the correlation gap satisfies

$$R^{2D}_{mm'}(dx, dy) - R^{3D}_{mm'}(dx, dy, dz) \geq 1 - \sqrt{\frac{1}{2}(1 + J_0(4\pi dz))}, \quad (26)$$

and is a tight lower bound for $dz \ll 1$.

Proof: See Appendix C.

The bound in (26) is verified in Fig. 6, where $R^{3D}_{mm'}$, $R^{2D}_{mm'}$ and the lower bound are shown for increasing dz. We note that the SC predicted by the 3D model decreases rapidly with dz and (26) provides a simple yet accurate method of correcting the 2D SC value for vertical separations up to $dz = 0.2\lambda$. Collectively, we have shown that the case $dz = 0$ and $A_V(\theta) = 1$ will lead to $R^{3D}_{mm'}(dx, dy, 0) \geq R^{2D}_{mm'}(dx, dy)$ due to a smaller equivalent spacing $(dx \sin\theta, dy \sin\theta)$ for 3D SC. However, by including the terms $A_V(\theta)$ and $e^{j2\pi dz \cos\theta}$, 3D SC will deceases rapidly and will be lower, sometimes much lower, than 2D SC.

C. Decomposition of $R^{3D}_{mm'}$

Using (23), the approximation, $R^{2D}_{mm'}(dx \sin\theta, dy \sin\theta) \approx R^{2D}_{mm'}(dx, dy)$, allows us to write

$$R^{3D}_{mm'}(dx, dy, dz) = R^{el}_{mm'}(dz) R^{2D}_{mm'}(dx, dy), \quad (27)$$

where the SC due to elevation distance is

$$R^{el}_{mm'}(dz) = \frac{\mathbb{E}_\theta\{A_V(\theta) e^{-j2\pi dz \cos\theta}\}}{\mathbb{E}\{A_V(\theta)\}}. \quad (28)$$

Thus, the SC matrix $\mathbf{R}_{3D}$ can be approximated by the product of the azimuth domain SC, $\mathbf{R}_{2D}$, and elevation domain SC, $\mathbf{R}_{el}$.

$$\mathbf{R}_{3D} \approx \mathbf{R}^{app}_{3D} = \mathbf{R}_{el} \odot \mathbf{R}_{2D}. \quad (29)$$

where the elements of $\mathbf{R}_{el}$ are obtained from (28). The accuracy of the approximate SC, $\mathbf{R}^{app}_{3D}$ in (29), is validated in terms of channel capacity in the next section.

D. Impact of SC Model on Capacity

Finally, we evaluate the impact of including the effects of 3D channel SC on the predicted MIMO capacity performance. For this purpose, we consider a 8×8 MIMO system with rectangular cross polarized antenna configuration at both Tx and Rx. We assume the Kronecker SC model for a simple

Rayleigh fading channel

$$\mathbf{H} = \mathbf{R}_{\text{Rx}}^{1/2}\mathbf{G}\mathbf{R}_{\text{Tx}}^{1/2}, \tag{30}$$

where $\mathbf{G} \in \mathcal{C}^{Q\times M}$ has $\mathcal{CN}(0,1)$ entries. The Tx and Rx SC matrices $\mathbf{R}_{\text{Tx}}$ and $\mathbf{R}_{\text{Rx}}$ have their entries computed from (18) and (17) for 2D and 3D SC models, respectively. We also consider the approximate decoupled SC expression in (29). From (30), the capacity is computed using

$$C = \mathbb{E}\left\{\log_2 \det\left(\mathbf{I} + \frac{\text{SNR}}{\beta M}\mathbf{H}^{\text{H}}\mathbf{H}\right)\right\}, \tag{31}$$

where β is the normalization factor such that

$$\mathbb{E}\left\{\frac{1}{\beta}||\mathbf{H}||_{\text{F}}^2\right\} = MQ. \tag{32}$$

Assuming $\theta \sim \mathcal{U}[0,\pi]$ and $\phi \sim \mathcal{U}[-\pi,\pi]$, Fig. 7 shows the capacity results for the three SC models $\mathbf{R}_{\text{2D}}, \mathbf{R}_{\text{3D}}$ and $\mathbf{R}_{\text{3D}}^{\text{app}}$ with antenna separation (dx, dy, dz) as indicated in the legend. We observe a large capacity gap between $\mathbf{R}_{\text{2D}}$ and $\mathbf{R}_{\text{3D}}$ for $dy = dz = 0.5\lambda$. Using a 2D model underestimates the system capacity by 62% at SNR $= 5$ dB, as it does not include the degrees of freedom resulting from the elevation angle spread. The accuracy of $\mathbf{R}_{\text{3D}}$ decomposition in (29) is validated as the capacity curve of $\mathbf{R}_{\text{3D}}^{\text{app}}$ stays close to that of $\mathbf{R}_{\text{3D}}$.

V. Conclusion

In this paper, new spatial correlation expressions for rectangular arrays of cross-polarized antennas with 3D and 2D channel models have been derived. We relate SC in 2D and 3D models and show that 2D SC can be regarded as a special case of 3D SC when elevation interval spacing is zero and elevation angle is fixed at $\pi/2$. It's also shown that the antenna radiation pattern and elevation interval spacing contribute greatly to a lower 3D SC. Furthermore, we quantify the effects of the elevation domain (both elevation angle spread and interval spacing) on SC. For a small elevation angle spread, the above gap grows quadratically in both vertical separation and angle spread. For the case of small vertical spacing, a tight bound on the above correlation gap has been derived. Then we have decoupled the elevation effects on correlation and express the 3D SC matrix as a Hadamard product of a 2D SC matrix and an elevation component. Finally, a channel capacity result is included based on the above SCs to validate that differences in correlation structure can create performance differences of the same scale as seen in measurements (see Fig. 1). The capacity results also show the accuracy of decomposing 3D SC into elevation and azimuth components. Through the analysis, we have highlighted the need for accurate channel modeling when evaluating the performance of 3D MIMO systems.

VI. Appendices

A. Derivation of 3D SC

Beginning with (14), we see that

$$\mathbb{E}\left\{\boldsymbol{h}_m^*\boldsymbol{h}_{m'}\right\} = \frac{Q}{2CL}\sum_{c=1}^{C}\sum_{l=1}^{L}\mathbb{E}\left\{P_{q,m}^*P_{q,m} + P_{q_\perp,m}^*P_{q_\perp,m}\right\} \mathbb{E}\left\{A(\theta_{c,l},\phi_{c,l})e^{j2\pi(\boldsymbol{d_m}-\boldsymbol{d_{m'}})}\right\}\mathbb{E}\left\{A(\vartheta_{c,l},\varphi_{c,l})\right\}. \tag{33}$$

Using (34) (on the next page, where $I(\alpha_i^*\alpha_j)$ denotes the cross terms of α_i^* and α_j), we obtain

$$\begin{aligned}\mathbb{E}\{P_{q,m}^*P_{q,m} + P_{q_\perp,m}^*P_{q_\perp,m'}\} &= (1+\kappa^{-1})(\cos\xi_m\cos\xi_m^{'} + \sin\xi_m\sin\xi_m^{'}) \\ &= (1+\kappa^{-1})\cos(\xi_m - \xi_m^{'}).\end{aligned} \tag{35}$$

We note that for $|\xi_m - \xi_m^{'}| = \frac{\pi}{2}$, $\mathbb{E}\{\boldsymbol{h}_m^*\boldsymbol{h}_{m'}\} = 0$. For $\xi_m = \xi_m^{'}$, substituting (35) into (33) gives

$$\mathbb{E}\{\boldsymbol{h}_m^*\boldsymbol{h}_{m'}\} = \frac{Q(1+\kappa^{-1})}{2CL}\sum_{c=1}^{C}\sum_{l=1}^{L}\mathbb{E}\{A_te^{j2\pi(\boldsymbol{d_m}-\boldsymbol{d_{m'}})}\}\mathbb{E}\{A_r\}. \tag{36}$$

For $m = m'$

$$\mathbb{E}\{||\boldsymbol{h}_m||^2\} = \frac{Q(1+\kappa^{-1})}{2CL}\sum_{c=1}^{C}\sum_{l=1}^{L}\mathbb{E}\{A_t\}\mathbb{E}\{A_r\}, \tag{37}$$

where $A_t = A(\theta_{c,l},\phi_{c,l})$, and $A_r = A(\vartheta_{c,l},\varphi_{c,l})$. As cluster angles are assumed i.i.d, (36) and (37) can be simplified to

$$\mathbb{E}\{\boldsymbol{h}_m^*\boldsymbol{h}_{m'}\} = \frac{Q}{2}(1+\kappa^{-1})\mathbb{E}\{A(\theta,\phi)e^{j2\pi(\boldsymbol{d_m}-\boldsymbol{d_{m'}})}\}\mathbb{E}\{A(\vartheta,\varphi)\}, \tag{38}$$

$$\mathbb{E}\{||\boldsymbol{h}_m||^2\} = Q(1+\kappa^{-1})\mathbb{E}\{A(\theta,\phi)\}\mathbb{E}\{A(\vartheta,\varphi)\}. \tag{39}$$

Substituting (38) and (39) into (16) results in

$$R_{mm'}^{\text{3D}} = \frac{\mathbb{E}\{A(\theta,\phi)e^{-j2\pi\boldsymbol{r}_{\text{Tx}}^T(\boldsymbol{d}_m-\boldsymbol{d}_{m'})}\}}{\mathbb{E}\{A(\theta,\phi)\}} \quad \text{for} \quad \xi_m = \xi_{m'}, \tag{40}$$

B. Proof of Lemma 1

Let θ lie within a small range near $\pi/2$, ie., $\theta = \pi/2 + \delta$ where δ is within $(-\varepsilon,\varepsilon)$ and $\theta \sim \mathcal{U}(\frac{\pi}{2}-\varepsilon, \frac{\pi}{2}+\varepsilon)$. Using Taylor series expansion at $\theta = \pi/2$, we have

$$\begin{aligned}\cos\theta &= \cos(\frac{\pi}{2}+\delta) = -\sin(\delta) \approx -\delta + O(\delta^3), \\ \sin\theta &= \sin(\frac{\pi}{2}+\delta) = \cos(\delta) \approx 1 - \frac{1}{2}\varepsilon^2 + O(\delta^4),\end{aligned} \tag{41}$$

$$e^{-j2\pi dz\cos\theta} \approx 1 + j2\pi dz\delta - \frac{(2\pi dz)^2}{2}\delta^2 + O(\delta^2), \tag{42}$$

$$A_V(\theta) = e^{-k_0\delta^2} \approx 1 - k_0\delta^2 + O(\delta^2), \tag{43}$$

where $k_0 = 12(\frac{180}{65\pi})^2\frac{\ln 10}{10}$. Using (41), we have

$$\begin{aligned}&R_{mm'}^{\text{2D}}(dx\sin\theta, dy\sin\theta) = R_{mm'}^{\text{2D}}(dx+\Delta x, dy+\Delta y), \\ &\frac{R_{mm'}^{\text{2D}}(dx+\Delta x, dy+\Delta y) - R_{mm'}^{\text{2D}}(dx,dy)}{\Delta x\Delta y} \approx \frac{\partial^2 R_{mm'}^{\text{2D}}(dx,dy)}{\partial dx\partial dy},\end{aligned} \tag{44}$$

where

$$\Delta x = -\frac{dx}{2}\delta^2 + O(\delta^4), \quad \Delta y = -\frac{dy}{2}\delta^2 + O(\delta^4), \tag{45}$$

Using (44) and (45), we have

$$\begin{aligned}&R_{mm'}^{\text{2D}}(dx+\Delta x, dy+\Delta y) \\ &\approx R_{mm'}^{\text{2D}}(dx,dy) + \frac{\partial^2 R_{mm'}^{\text{2D}}(dx,dy)}{\partial dx\partial dy}\Delta x\Delta y \\ &\approx R_{mm'}^{\text{2D}}(dx,dy) + k_1\delta^4 + O(\delta^4).\end{aligned} \tag{46}$$

$$\begin{cases} E\left\{P^*_{q,m}P_{q,m'}\right\} = E\left\{||\alpha_{VV}||^2 \cos\xi_q{}^2 \cos\xi_m \cos\xi_{m'} + ||\alpha_{VH}||^2 \cos\xi_q{}^2 \sin\xi_m \sin\xi_{m'}\right. \\ \qquad\qquad \left. + ||\alpha_{HV}||^2 \sin\xi_q{}^2 \cos\xi_m \cos\xi_{m'} + ||\alpha_{HH}||^2 \sin\xi_q{}^2 \sin\xi_m \sin\xi_{m'} + I(\alpha_i^*\alpha_j)\right\} \\ \qquad\qquad = \cos\xi_q{}^2 \cos\xi_m \cos\xi_{m'} + \sin\xi_q{}^2 \sin\xi_m \sin\xi_{m'} + \kappa^{-1}(\cos\xi_q{}^2 \sin\xi_m \sin\xi_{m'} + \sin\xi_q{}^2 \cos\xi_m \cos\xi_{m'}) \\ E\left\{P^*_{q_\perp,m}P_{q_\perp,m'}\right\} = E\left\{||\alpha_{VV}||^2 \sin\xi_q{}^2 \cos\xi_m \cos\xi_{m'} + ||\alpha_{VH}||^2 \sin\xi_q{}^2 \sin\xi_m \sin\xi_{m'}\right. \\ \qquad\qquad \left. + ||\alpha_{HV}||^2 \sin\xi_q{}^2 \cos\xi_m \cos\xi_{m'} + ||\alpha_{HH}||^2 \sin\xi_q{}^2 \sin\xi_m \sin\xi_{m'} + I(\alpha_i^*\alpha_j)\right\} \\ \qquad\qquad = \sin\xi_q{}^2 \cos\xi_m \cos\xi_{m'} + \cos\xi_q{}^2 \sin\xi_m \sin\xi_{m'} + \kappa^{-1}(\sin\xi_q{}^2 \sin\xi_m \sin\xi_{m'} + \cos\xi_q{}^2 \cos\xi_m \cos\xi_{m'}) \end{cases} \tag{34}$$

$$\begin{aligned} R^{\text{3D}}_{mm'}(dx,dy,dz) &\approx \frac{\mathbb{E}\left\{\left[1-(k_0^2\ln 10/10)\delta^2\right]\left[1+j2\pi dz\delta-\frac{(2\pi dz)^2}{2}\delta^2\right]\left[R^{\text{2D}}_{mm'}(dx,dy)+k_1\delta^4\right]\right\}}{\mathbb{E}\left\{1-(k_0^2\ln 10/10)\delta^2\right\}} \\ &\approx \frac{R^{\text{2D}}_{mm'}(dx,dy)\mathbb{E}\left[1+j2\pi dz(\delta)-\frac{(2\pi dz)^2}{2}\delta^2-(k_0^2\ln 10)\delta^2+O(\delta^2)\right]}{\mathbb{E}\{1-(k_0^2\ln 10/10)\delta^2\}} \\ &= \frac{R^{\text{2D}}_{mm'}(dx,dy)\int_{-\varepsilon}^{\varepsilon}\left[1-\frac{(2\pi dz)^2}{2}\delta^2-(k_0^2\ln 10/10)\delta^2\right]\frac{1}{2\varepsilon}d\delta}{\int_{-\varepsilon}^{\varepsilon}\left[1-(k_0^2\ln 10/10)\delta^2\right]\frac{1}{2\varepsilon}d\delta} \\ &\approx R^{\text{2D}}_{mm'}(dx,dy)\left[1-\frac{2(\pi dz)^2}{3}\varepsilon^2\right] \end{aligned} \tag{47}$$

where $k_1 = \frac{\partial^2 R^{\text{2D}}_{mm'}(dx,dy)}{\partial dx \partial dy}(\frac{dx}{2})(\frac{dy}{2})$. Substituting (42), (43) and (46) into (23) gives (47), which results in (25).

C. Proof of Lemma 2

First, we assume $A_V(\theta) = 1$ since this tends to increase $R^{\text{3D}}_{mm'}$ (see Fig. 4). Hence, this assumption leads to an upper bound and also simplifies the solution. For $f(\theta) \sim \mathcal{U}(0,\pi)$, using (23) we have

$$\begin{aligned} &R^{\text{3D}}_{mm'}(dx,dy,dz) \\ &= \frac{1}{\pi}\int_0^\pi e^{-j2\pi dz\cos\theta} R^{\text{2D}}_{mm'}(dx\sin\theta, dy\sin\theta)d\theta \\ &= \frac{1}{\pi}\int_0^\pi \cos(2\pi dz\cos\theta) R^{\text{2D}}_{mm'}(dx\sin\theta, dy\sin\theta)d\theta \\ &\le \frac{1}{\pi}\sqrt{\int_0^\pi \cos(2\pi dz\cos\theta)^2 d\theta \int_0^\pi R^{\text{2D}}_{mm'}(dx\sin\theta, dy\sin\theta)^2 d\theta} \\ &\le \frac{1}{\pi}\sqrt{\int_0^\pi \cos(2\pi dz\cos\theta)^2 d\theta \int_0^\pi 1 d\theta} \\ &= \sqrt{\frac{1}{2}(1+J_0(4\pi dz))}. \end{aligned} \tag{48}$$

Since the 2D correlation is unity, this completes the proof.

VII. Acknowledgement

This research is supported in part by National Natural Science Foundation of China and project Ultra-dense network for 5G with the MTC application with NO. 6141101115, and by 863 program under grant NO. 2014AA01A705.

References

[1] ITU-R, "Framework and overall objectives of the future development of IMT for 2020 and beyond," *San Diego, USA*, 10-18 June 2015.

[2] J. G. Andrews, S. Buzzi, W. Choi, S. V. Hanly, A. Lozano, A. C. Soong, and J. C. Zhang, "What will 5G be?," *IEEE Journal on Selected Areas in Communications*, vol. 32, no. 6, pp. 1065–1082, 2014.

[3] 3GPP TR 36.873 V.2, "Study on 3D channel model for LTE (Release 12)," Technical Report, 2014.

[4] ITU-R M.2135, "Guidelines for evaluation of radio interface technologies for IMT-Advanced," Technical Report, 2008.

[5] Y.-H. Nam, B. L. Ng, K. Sayana, Y. Li, J. Zhang, Y. Kim, and J. Lee, "Full-dimension MIMO (FD-MIMO) for next generation cellular technology," *IEEE Communications Magazine*, vol. 51, no. 6, pp. 172–179, 2013.

[6] Y. Yu, J. Zhang, and M. Shafi, "3D vs. 2D channel capacity of outdoor to indoor scenarios derived from measurements in China and New Zealand," in *2016 24th European Signal Processing Conference (EUSIPCO 2016)*, pp. 1980–1984, Aug 2016.

[7] A. Forenza, D. J. Love, and R. W. Heath, "Simplified spatial correlation models for clustered MIMO channels with different array configurations," *IEEE Transactions on Vehicular Technology*, vol. 56, no. 4, pp. 1924–1934, 2007.

[8] W. J. Queiroz, F. Madeiro, W. T. A. Lopes, and M. S. Alencar, "Spatial correlation for DoA characterization using Von Mises, cosine, and Gaussian distributions," *International Journal of Antennas and Propagation*, vol. 2011, 2011.

[9] K. Mammasis and R. Stewart, "Spherical statistics and spatial correlation for multielement antenna systems," *EURASIP Journal on Wireless Communications and Networking*, vol. 2010, no. 1, p. 1, 2010.

[10] S. K. Yong and J. S. Thompson, "Three-dimensional spatial fading correlation models for compact MIMO receivers," *IEEE Transactions on Wireless Communications*, vol. 4, no. 6, pp. 2856–2869, 2005.

[11] A. Kammoun, M. Debbah, M.-S. Alouini, *et al.*, "A generalized spatial correlation model for 3D MIMO channels based on the Fourier coefficients of power spectrums," *IEEE Transactions on Signal Processing*, vol. 63, no. 14, pp. 3671–3686, 2015.